Acta Materialia 199 (2020) 530–541

Contents lists available at ScienceDirect

Acta Materialia

journal homepage: www.elsevier.com/locate/actamat

Full length article

Ultrahigh temperature *in situ* transmission electron microscopy based bicrystal coble creep in zirconia I: Nanowire growth and interfacial diffusivity

K.S.N. Vikrant[a], Robson L. Grosso[b,c,d], Lin Feng[e], Eliana N.S. Muccillo[c], Dereck N.F. Muche[d], Gowtham S. Jawaharram[b], Christopher M. Barr[f], Anthony M. Monterrosa[f], Ricardo H.R. Castro[d], R. Edwin García[a], Khalid Hattar[f], Shen J. Dillon[b,*]

[a] School of Materials Engineering, Purdue University, West Lafayette, IN 47907, United States
[b] Department of Materials Science and Engineering, University of Illinois Urbana-Champaign, Urbana, IL 61801, United States
[c] Energy and Nuclear Research Institute, S. Paulo, PO Box 11049, Brazil
[d] Department of Materials Science and Engineering, University of California - Davis, California, 95616, United States
[e] School of Chemical Engineering and Technology, Sun Yat-sen University, Zhuhai, 519082, China
[f] Materials, Physical, and Chemical Sciences, Sandia National Laboratories, Albuquerque, NM 87185, United States

ARTICLE INFO

Article history:
Received 17 February 2020
Revised 12 July 2020
Accepted 24 August 2020
Available online 28 August 2020

Keywords:
in situ
Electron microscopy
Creep
ZrO_2

ABSTRACT

This work demonstrates novel *in situ* transmission electron microscopy-based microscale single grain boundary Coble creep experiments used to grow nanowires through a solid-state process in cubic ZrO_2 between ≈ 1200 °C and ≈ 2100 °C. Experiments indicate Coble creep drives the formation of nanowires from asperity contacts during tensile displacement, which is confirmed by phase field simulations. The experiments also facilitate efficient measurement of grain boundary diffusivity and surface diffusivity. 10 mol% Sc_2O_3 doped ZrO_2 is found to have a cation grain boundary diffusivity of $D_{gb} = (0.056 \pm 0.05)\exp(\frac{-380.000 \pm 41.000}{RT})m^2\ s^{-1}$, and surface diffusivity of $D_s = (0.10 \pm 0.27)\exp(\frac{-380.000 \pm 28.000}{RT})m^2\ s^{-1}$.

1. Introduction

Time-dependent interface mediated deformation via Coble creep occurs when atomic planes are removed from interfaces under relative compression and deposited on interfaces under relative tension [1]. Classically, the model has been applied to the deformation response of polycrystals at high homologous temperatures and fine grain sizes [2]. In the limit of the simplest microstructure susceptible to Coble creep, a bicrystal, the atomic flux will occur between the surface and the single grain boundary. A grain boundary in tension should produce filamentary growth of width determined by the characteristic diffusion distance of the rate limiting species. Coble creep, therefore, provides a solid-state route to produce free standing nanowires at appropriate temperatures. A solid-state deformation process has potential benefits over vapor-phase or solution-based methods due to the inherently lower entropy, which is favorable for obtaining desired chemistry and reducing the incorporation of impurities [3,4]. The universality of this deformation mechanism to crystalline solids implies that it should be suitable to prepare nanowires from any stable crystalline systems. Employing precision micromanipulation would enable deterministic placement of single nanowires or controlled nanowire arrays. However, observations of related phenomena are, too the authors' knowledge, limited.

Coble creep also provides a valuable tool for assessing interface diffusivity [5,6], a property whose measurement is typically laborious. Polycrystalline microstructures, however, often complicate the calculation of diffusivity [1,7]. The process, in theory, provides a basis for measuring fundamental aspects of transport at the nanoscale in addition to its ability to produce novel nanostructures. Bicrystalline Coble creep has not been the subject of significant investigation, likely due to scaling laws that suggest its relevance only at the microscale or nanoscale during timescales accessible to laboratory experiments [8]. Related experiments, therefore, require small scale manipulation and testing of specimens.

* Corresponding author.
E-mail address: sdillon@illinois.edu (S.J. Dillon).

https://doi.org/10.1016/j.actamat.2020.08.069
1359-6454/

Glossary of Symbols

f	Helmholtz free energy per unit volume (J/m^3)
$[V_j^{Z_j}]$	Mole fraction of j-th chemical species (–)
$[Sc'_{Zr}]$	Mole fraction of Scandium defects (–)
$[V_O^{\cdot\cdot}]$	Mole fraction of Oxygen vacancies (–)
η_i	Structural order parameter (–)
$\eta_\times$	Order parameter for solid crystalline lattice (–)
η_d	Order parameter for structurally disorder region (–)
η_v	Order parameter for open and closed porosity (–)
ρ	Local charge density (C/m^3)
ϕ	Electrostatic potential (V)
Z_j	Valence of j-th chemical species (–)
T	Temperature (K)
k_b	Boltzmann Constant (eV/atom)
$f^d_{V_O^{\cdot\cdot}} - f^X_{V_O^{\cdot\cdot}}$	Segregation energy of oxygen vacancies to grain boundary (eV)
$f^v_{V_O^{\cdot\cdot}} - f^X_{V_O^{\cdot\cdot}}$	Segregation energy of oxygen-vacancies to surface (eV)
$f^d_{Sc'_{Zr}} - f^X_{Sc'_{Zr}}$	Segregation energy of scandium defects to grain boundary (eV)
$f^v_{Sc'_{Zr}} - f^X_{Sc'_{Zr}}$	Segregation energy of scandium defects to surface (eV)
$w_{\times\, d}$	Energy barrier between order-disorder phases (J/m^3)
w_{dv}	Energy barrier between disorder-porous phases (J/m^3)
$w_{v\,\times}$	Energy barrier between order-porous phases (J/m^3)
$\Omega_{Sc'_{Zr}V_O^{\cdot\cdot}}$	Interaction parameter (eV)
$\Delta H^{\times \rightarrow d}$	Latent heat of fusion (J/m^3)
T_m	Melting temperature (K)
$\in$	Dielectric constant (F/m)
$\vec{E}$	Electric field (V/m)
σ_{ij}	ij-th component of stress tensor (N/m^2)
C_{ijkl}	Component of stiffness matrix (N/m^2)
ε_{ij}	ij-th component of strain tensor (–)
β^m_{ij}	ij-th component of Vegard tensor of m-th species (–)
$[V_m^{Z_m}]_o$	Stress free mole fraction of m-th species (–)
$\vec{u}$	Mechanical displacement (m)
$\overleftrightarrow{\sigma}$	Stress tensor (N/m^2)
$\overleftrightarrow{\varepsilon}_e$	Strain tensor (–)
$\overleftrightarrow{\beta}^j$	Vegard tensor of j-th species (–)
F	Total Helmholtz free energy (J)
θ	Crystallographic orientation (degree)
$\alpha_\times$	Grain boundary energy coefficient of order-disorder interface (J/m)
α_d	Grain boundary energy coefficient of disorder-porous interface (J/m)
α_v	Grain boundary energy coefficient of order-porous interface (J/m)
s_1	Structural coupling parameter (J/m^2)
s_1	Structural coupling parameter (J/m)
$g(\eta_\times)$	Coupling function (–)
$p(\eta_i)$	Interpolation function (–)
$\vec{v}$	Velocity (m/s)
$M_{\eta_\times}$	Kinetic coefficient for crystalline transformation (m/Js^3)
M_θ	Kinetic coefficient for orientation transformation (m/Js^3)
M_{η_v}	Mobility of porous phase (m^5/Js^3)
M_j	Mobility of j-th species (m^5/Js^3)
ρ_m	Condensed phase (–)

The current work focuses on measuring the interfacial kinetics and thermodynamics of cubic ZrO_2 bicrystals during nanowire growth. ZrO_2 ranks amongst the most important ceramic materials; serving as the prototypical oxygen ion conductor [9–11], an ideal thermal barrier coating for high temperature applications [12], and a mechanically robust structural oxide [13]. The creep rate of polycrystalline ZrO_2 has been measured in multiple prior studies. [14–18] Grain boundary and surface transport of cations, primarily investigated in this work, affects the microstructural and mechanical stability of porous thermal barrier coatings, [19,20] the pressure induced formation of pores in solid oxide electrolyzer cells, [21] and the sintering kinetics of ZrO_2 ceramics [22,23]. Experimental reports of tetravalent cation diffusion, e.g. Zr^{4+} or Hf^{4+}, in different doped ZrO_2 samples vary by ≈3 orders of magnitude at a single temperature. [24–34] The large variations in reported grain boundary diffusivities have not been completely rationalized. Obtaining accurate grain boundary tracer diffusivities from extrinsic oxides sensitive to dopants and impurities is challenging in the so-called Harrison's type B regime, where lattice diffusivity must be known to calculate grain boundary values. [35] Lattice diffusivities are typically obtained from single crystals of inherently different chemistry than the polycystals or from fitting the near surface portion of composition depth profiles, which often produces spurious results. Measurements of grain boundary diffusivity independent of lattice diffusivity are, therefore, desirable particularly in oxides that have impurity sensitive lattice diffusivities [36]

The current authors recently applied a combination of laser heating and small-scale mechanical testing to ultra-high temperature mechanical testing of ZrO_2 with an emphasis on yield strength determination and the role of temperature and microstructure in affecting this property. [37] This manuscript extends high temperature mechanical testing to investigation of single grain boundary Coble creep. The ability to measure grain boundary diffusivity, the stress dependence, as well as the energy dissipated during creep in a model single grain boundary system provides a robust set of experimental data describing interfacial kinetics and thermodynamics. For this reason, the current work is separated into two parts. This manuscript emphasizes measurement of interfacial diffusivity during and after bicrystal Coble creep and uses phase-field simulations to provide independent validation of the proposed mechanism. A companion paper uses data from this series of experiments to measure interfacial energies as well as the formation and migration volumes for the grain boundary diffusion mediating point defects. [38] The thermodynamic and kinetic data from both texts are then applied in the companion paper to the problem of understanding the mechanism for densification during sintering [38].

2. Experimental

Dense 10%Sc_2O_3 doped ZrO_2 (10ScSZ) samples were prepared following a procedure detailed elsewhere. [39,40] A focused ion beam (FIB) was used to prepare pillar shaped samples of dimension ≈ 500 nm x 500 nm x 600 nm. The samples were pre-annealed *in situ* at T ≈ 2000 °C for ≈15 min, which allowed the shape of the pillar to relax, the grain size to coarsen to d>20 μm resulting in single crystalline asperities, and evaporation of any minor Ga_2O_3 contaminant introduced during FIB preparation, T_{boil} ≈

1900 °C. Ion beam deposited Pt was deposited in the adjacent ≈ 50 μm to enhance optical absorption but was found to have evaporated during the high temperature experiments; suggesting that it was not critical to the heating process. A 1064 nm 20 W laser with an ≈ 100 μm spot size was used to heat the sample. The temperature was determined in part from electron diffraction-based measurements of lattice parameter expansion, a_o, referenced to prior x-ray based measurements reported in the literature. [41] Prior *in situ* laser heating experiments using both diffraction and 4-probe electrical resistance measurements indicate sample heating is reasonably linear at applied powers beyond P > 1.5 W, which slightly exceeds the threshold for emission P > 1.4 W. [42] The onset of laser emission, the rhombohedral to cubic phase transition, and the melting temperature were also used as references to calibrate the temperature as a function of laser power assuming linear response; an assumption supported by the diffraction data and prior experiments performed in the same microscope. The onset of grain growth and the onset of surface diffusion mediated changes in pillar shape were also used as secondary reference points to support the calibration. [43] These data provide independent confirmation of the overall calibration curves constructed; see Figure S1.

The bicrystals were formed using two different sample sets. In one case 10ScSZ asperities were sintered *in situ* to an 8%Y_2O_3 doped ZrO_2 (8YSZ) single crystal, and in a second set of experiments it was sintered to another 10ScSZ prepared from the same bulk sample. The samples will subsequently be described as YSZ-ScSZ and ScSZ-ScSZ. The opposing samples in the bicrystal were prepared in a similar manner as described above, via FIB and Pt deposition, but with a larger contact diameter, ≈ 10 μm for 8YSZ and ≈ 50 μm for 10ScSZ. Both samples were prepared from bulk material approximately 2 mm in length and wedge polished to 20-40 μm in thickness. The single crystal 8YSZ enabled testing of the same bicrystal over multiple experiments, whereas the 10ScSZ was polycrystalline and enabled the testing of random grain boundaries. The 8YSZ based bicrystal formed a 'general' type boundary with a misorientation of 21 º about the [1 $\bar{1}$ 16]; as measured by electron diffraction. The temperature of the 8YSZ was found to be slightly lower, ≈ 100 °C, when measured out-of-contact, possibly due to differences in optical absorption or thermal impedances between opposite sides of the holder. This amount of temperature difference produces at most a systematic error of ≈4-7% in the temperature determination, although it may be reasonable to expect the error is intermediate to the maximum difference; i.e. an error of ≈2-4%. This error is an addition to any errors introduced by the calibration.

Experiments were performed in a 200 kV JEOL 2100 using a Bruker PI-95 picoindenter. The laser is set in colinear alignment with the electron beam. Samples were tested in tension using displacement rates varying between 0.5 nm s^{-1} and 1000 nm s^{-1}. Two types of experiment were performed; one in which the sample was allowed to sinter for > 30 s prior to tensile loading, i.e. YSZ-ScSZ experiments, and one in which tensile loading was applied just after contact; the ScSZ-ScSZ experiments. The first type of experiment provides time for a relatively large grain boundary neck to form at the contact, while the latter does not. The large neck allows for accurate measurement of the stress-strain response, but many of those samples ultimately fracture rather than exhibit steady-state creep under displacement control. ScSZ-ScSZ were rested without pre-sintering to ensure that they would creep for all experiments performed below a threshold displacement rate determined by the rate limiting diffusion process. The laser repetition rate, 33 kHz, is fast relative to the thermal relaxation time of the sample, due to its high thermal impedance. Equilibration of the sample temperature required times on the order of 10 minutes, which was determined to have occurred when thermal expansion ceased to be observable at the nanoscale. At this point the sample temperature will have reached a steady-state. Experiments were performed using a load-displacement data acquisition rate of ≈ 200 Hz and an *in situ* image acquisition rate of ≈ 15 Hz (Tietz video and image processing system). Electron irradiations performed on ZrO_2 reveal that the threshold electron energy for displacement damage only occurs at ≈ 1 MeV. [44] Thus, it is concluded that electron irradiation in our experiments, at 200 keV, should not induce displacement damage that could affect diffusion. Furthermore, electron beam induced heating at the beam current densities employed is calculated to be at most on the order of 1 º C and should not influence the temperature significantly. The resulting images were analyzed using ImageJ. Local curvature of particles was calculated using the compute curvatures algorithm in Image J. [45] The areas, lengths, and geometric alignment of ellipses fitted to image features were determined using ellipse split in Image J. [46] Data based on measurements of distance in the TEM images are reported at 2 significant figures since the pixel size in most images is on the order of 5 nm.

3. Simulation

3.1. Theoretical Framework

Following previous work [47–49], Helmholtz free energy per unit volume, f, is defined for an ionic solid with N charged species, $\{[V_j^{Z_j}]\} = \{[V_1^{Z_1}], \ldots, [V_N^{Z_N}]$, and three distinct microstructural regions, $\{\eta_i\} = \{\eta_\times, \eta_d, \eta_v\}$, where, $\eta_\times$, is the solid crystalline lattice, η_d, is the structurally disordered regions, and η_v, represents open and closed porosity. The volumetric chemical and structural free energy density is:

$$f\left(\{\eta_i\},\ \left[Sc_{Zr}^{'}\right],\ [V_O^{\cdot\cdot}];T\right) = \frac{1}{\nu}\Big[(f_{V_O^{\cdot\cdot}}^{\times}(T)p(\eta_\times) + f_{V_O^{\cdot\cdot}}^{d}(T)p(\eta_d) + f_{V_O^{\cdot\cdot}}^{v}(T)p(\eta_v))[V_O^{\cdot\cdot}] + \left(f_{Sc_{Zr}^{'}}^{X}(T)p(\eta_\times) + f_{Sc_{Zr}^{'}}^{d}(T)p(\eta_d) + f_{Sc_{Zr}^{'}}^{v}(T)p(\eta_v)\right)\left[Sc_{Zr}^{'}\right] + k_bT[V_O^{\cdot\cdot}]\log[V_O^{\cdot\cdot}] + k_bT(1-[V_O^{\cdot\cdot}])(1-\log[V_O^{\cdot\cdot}]) + k_bT\left[Sc_{Zr}^{'}\right]\log\left[Sc_{Zr}^{'}\right] + k_bT\left(1-\left[Sc_{Zr}^{'}\right]\right)\left(1-\log\left[Sc_{Zr}^{'}\right]\right) + \Omega_{Sc_{Zr}^{'}V_O^{\cdot\cdot}}[V_O^{\cdot\cdot}]\left[Sc_{Zr}^{'}\right] + w_{\times d}\eta_\times^2\eta_d^2 + w_{dv}\eta_d^2\eta_v^2 + w_{v\times}\eta_v^2\eta_\times^2 + \frac{\Delta H^{\times\to d}\ \Delta T}{T_m}p(\eta_\times)\Big] \quad (1)$$

Each charged species has a valence of Z_j and contributes to the local charge density through the expression, $\rho = \sum_{j=1}^{N} eZ_j[V_j^{Z_j}]$, and a local electrostatic potential, ϕ. Further, the material is electrostatically polarized with a dielectric constant, $\in$, and a local electric field, $\vec{E} = -\nabla\phi$ [47,50]. Each charged species imposes a change in lattice parameter which develops an elastic stress following a modified Hooke's law: $\sigma_{ij} = C_{ijkl}(\varepsilon_{kl} - \sum_{i=1}^{N}\beta_{kl}^{m}([V_m^{Z_m}] - [V_m^{Z_m}]_o))$, [51], where β_{ij}^{m} is the ij-th component of the Vegard tensor for the m-th species. In the small deformation limit, the geometrical strain, ε_{ij}, and mechanical displacement, $\vec{u} = (u_1, u_2, u_3)^T$ are related through the expression: $\varepsilon_{ij} = \frac{1}{2}(\frac{\partial u_i}{\partial x_j} + \frac{\partial u_j}{\partial x_i})$. The segregation of each charged species, here, results in the development of elastic energy inhomogeneities, *i.e.*, $\frac{1}{2}\bar{\sigma}\cdot\bar{\varepsilon}_e \geq 0$.

The sum of all the contributions to the total free energy functional, F, including the grain boundary interfacial energy and external surfaces, as a function of local misorientation, $\Delta\theta$, is given by [47,49,51]:

$$F\left[\{\eta_i\},\ \theta, \left[Sc_{Zr}^{'}\right],\ [V_O^{\cdot\cdot}], \rho, \phi, u_1, u_2, u_3; T\right] = \int_\Omega \left[\begin{array}{c} f\left(\{\eta_i\},\ \left[Sc_{Zr}^{'}\right],\ [V_O^{\cdot\cdot}];T\right) + \frac{\alpha_\times^2}{2}(\nabla\eta_\times)^2 + \frac{\alpha_d^2}{2}(\nabla\eta_d)^2 + \frac{\alpha_v^2}{2}(\nabla\eta_v)^2 + \\ g(\eta_\times)\left(s_1|\nabla\theta| + s_2|\nabla\theta|^2\right) + \rho\phi - \frac{\in}{2}(\nabla\phi)^2 + \frac{1}{2}\bar{\sigma}\cdot\bar{\varepsilon}_e \end{array}\right] d\Omega \quad (2)$$

Table 1
Summary of physical parameters used in phase-field simulation.

Parameter	Symbol	Value	Units	Ref
Oxygen vacancies ionic valence	Z_O	2	–	–
Scandium defects ionic valence	Z_{Sc}	-1	–	–
Segregation energy of oxygen vacancies to grain boundary	$f^d_{V_O^{\cdot\cdot}} - f^X_{V_O^{\cdot\cdot}}$	-0.5	eV	[88]
Segregation energy of oxygen vacancies to surface	$f^v_{V_O^{\cdot\cdot}} - f^X_{V_O^{\cdot\cdot}}$	-0.5	eV	[88]
Segregation energy of scandium defects to grain boundary	$f^d_{Sc'_{Zr}} - f^X_{Sc'_{Zr}}$	0.0	eV	[88]
Segregation energy of scandium defects to surface	$f^v_{Sc'_{Zr}} - f^X_{Sc'_{Zr}}$	0.0	eV	[88]
Order-disorder interfacial energy	$\gamma_{\times d}$	1.67	J/m^2	
Order-porous interfacial energy	$\gamma_{\times v}$	1.34	J/m^2	
disorder-porous interfacial energy	γ_{dv}	1.34	J/m^2	
Interfacial thickness between order-disorder phases	$\delta_{\times d}$	1	nm	
Interfacial thickness between disorder-porous phases	δ_{dv}	1	nm	
Interfacial thickness between order-porous phases	$\delta_{\times v}$	1	nm	
Energy barrier between order-disorder phases	$w_{\times d}$	5×10^9	J/m^3	[52]
Energy barrier between disorder-porous phases	w_{dv}	4×10^9	J/m^3	[52]
Energy barrier between order-porous phases	$w_{\times v}$	4×10^9	J/m^3	[52]
Grain boundary energy coefficient of order-disorder interface	$\alpha_\times$	10×10^{-9}	J/m	[52]
Grain boundary energy coefficient of disorder-porous interface	α_v	8×10^{-9}	J/m	[52]
Grain boundary energy coefficient of order-porous interface	α_d	10×10^{-9}	J/m	[52]
Structural coupling parameter	s_1	9.2	J/m^2	[52]
Structural coupling parameter	s_2	0.008	J/m	[52]
Atomic volume of zirconia	ν	3.6×10^{-29}	m^3/atom	–
Latent heat of fusion	$\Delta H^{\times \rightarrow d}$	3.5×10^9	J/ m^3	–
Melting temperature	T_m	2988	K	–
Interaction parameter	$\Omega_{Sc'_{Zr}V_O^{\cdot\cdot}}$	-0.13	eV	[89]
Relative dielectric permittivity of ScSZ	$\in_r$	31.45	–	[90]
Relative dielectric permittivity of pores	$\in_\circ$	1	–	
Elastic Modulus	E	160	GPa	[91]
Vegard coefficient of scandium defects in zirconia lattice	$\beta_{Sc'_{Zr}}$	0.001	–	[90]
Kinetic coefficient for crystalline transformation	$M_{\eta_\times}$	3.5×10^{-8}	m/Js^3	[47,52]
Kinetic coefficient for orientation transformation	M_θ	3.6×10^{-7}	m/Js^3	[47,52]
Mobility of porous phase	M_{η_v}	7.02×10^{-28}	m^5/Js^3	[47,52]

Locally, for small deviations away from equilibrium, spatial inhomogeneities of the variational derivatives of the free energy functional of Eq. (2) with respect to the controlling variables, $\{\{\eta_i\}, \{[V_j^{Z_j}]\}, \theta, \phi, u_1, u_2, u_3\}$ result in the kinetic equations:

$$\begin{aligned}
&\frac{\partial \eta_\times}{\delta \eta} + \vec{v}\cdot\nabla\eta_\times = -M_{\eta_\times}\left[\frac{\partial f}{\partial \eta_\times} - \alpha_\times^2\nabla^2\eta_\times - \frac{\alpha_d^2}{2}\nabla^2\eta_v + \frac{\partial g}{\partial \eta_\times}\left(s_1|\nabla\theta| + \frac{s_2}{2}|\nabla\theta|^2\right)\right]\\
&\frac{\partial \theta}{\partial t} + \vec{v}\cdot\nabla\theta = M_\theta g(\eta_\times)\left(\nabla\cdot\left[s_1\frac{\nabla\theta}{|\nabla\theta|}\right] + s_2\nabla^2\theta\right)\\
&\frac{\partial \eta_v}{\partial t} + \vec{v}\cdot\nabla\eta_v = -M_{\eta_v}\left[\frac{\partial f}{\partial \eta_v} - \alpha_v^2\nabla^2\eta_v - \frac{\alpha_d^2}{2}\nabla^2\eta_\times\right]\\
&\frac{\partial\left[V_j^{Z_j}\right]}{\partial t} + \vec{v}\cdot\nabla\left[V_j^{Z_j}\right] = \nabla\cdot M_j\nabla\left[\frac{\partial f}{\partial\left[V_j^{Z_j}\right]} + Z_j e\phi - \bar{\sigma}\cdot\bar{\beta}^j\right]\\
&\frac{\delta F}{\delta\phi} = \nabla\cdot\in\nabla\phi + \rho = 0\\
&\frac{\delta F}{\delta u_i} = \nabla\cdot\bar{\sigma} = 0
\end{aligned} \tag{3}$$

The kinetic equations are coupled to the continuity equation in its differential form, $\frac{\partial \rho_m}{\partial t} + \nabla\cdot(\rho_m\vec{v}) = 0$, where $\rho_m = 1 - \eta_v$ is density of condensed phase, which is 1 in condensed phase and 0 in porous region, and $\vec{v} = \frac{d\vec{u}}{dt}$ is rate of change in mechanical displacement due to externally applied stresses or local chemomechanical stresses. The first row of Eq. (3) defines the non-conserved order-disorder phase transformation, $\eta_\times \rightarrow \eta_d$, and defines the kinetics of structural disorder, if any, in the elongated polycrystal. The second row corresponds to the crystallographic orientation kinetics in agreement with Kobayashi and coworkers [52]. The third row defines the porous phase, η_v, a conserved quantity. The concentration of solute and point defects in the condensed phase are conserved and follows convection-diffusion mass transport as shown in fourth row of Eq. (3), in agreement with several authors [47,49,50]. The gradients in local structure, electrical and mechanical stresses in convection-diffusion equation allow for mass and charge flow. The fifth row corresponds Coulomb's equation in its differential form. Lastly, the sixth row corresponds to the mechanical equilibrium equation, in agreement with continuum mechanics theory [51]. The terms, $\vec{v}\cdot\nabla\eta_\times$, $\vec{v}\cdot\nabla\theta$, $\vec{v}\cdot\nabla\eta_v$, $\vec{v}\cdot\nabla[V_j^{Z_j}]$, account for convective flow of the condensed, porous and chemical species in the Eq. (3), in agreement with recent work [53].

3.2. Numerical implementation

A two-dimensional indenter-substrate ScSZ bicrystals were simulated, (see Figure S2). The physical properties of ScSZ are summarized in Table 1. Initial $[V_{\ddot{O}}]$ and $[Sc'_{Zr}]$ were set to their macroscopic, experimentally reported equilibrium values, and set to zero in porous regions. Electrically, the bottom edge of the simulation domain was grounded. The indenter in the simulation domain was pulled vertically at a fixed velocity from the top edge, by removing mass from the top edge at a fixed rate. The bottom edge is mechanically constrained. Eq. (3) was solved across a $1\mu m \times 1\mu m$ domain and discretized into a 1000×1000 finite volume mesh, using FiPy [54]. The relative tolerance for convergence was set to 1×10^{-10}. The mechanical equilibrium of Eq. (3) was solved using OOF2 [55]. The relative tolerance for convergence was set to 1×10^{-8}. Simulations were carried out on a 2.6 GHz, 16 core, Ubuntu 16.04 workstation with 128 GB of RAM. Each simulation took approximately eight hours of wall time.

4. Results and discussion

4.1. Nanowire growth and grain boundary diffusivity

Fig. 1 shows time-lapse images of the YSZ-ScSZ and ScSZ-ScSZ samples tested at similar temperatures, $T = 1928$ °C and $T = 1975$

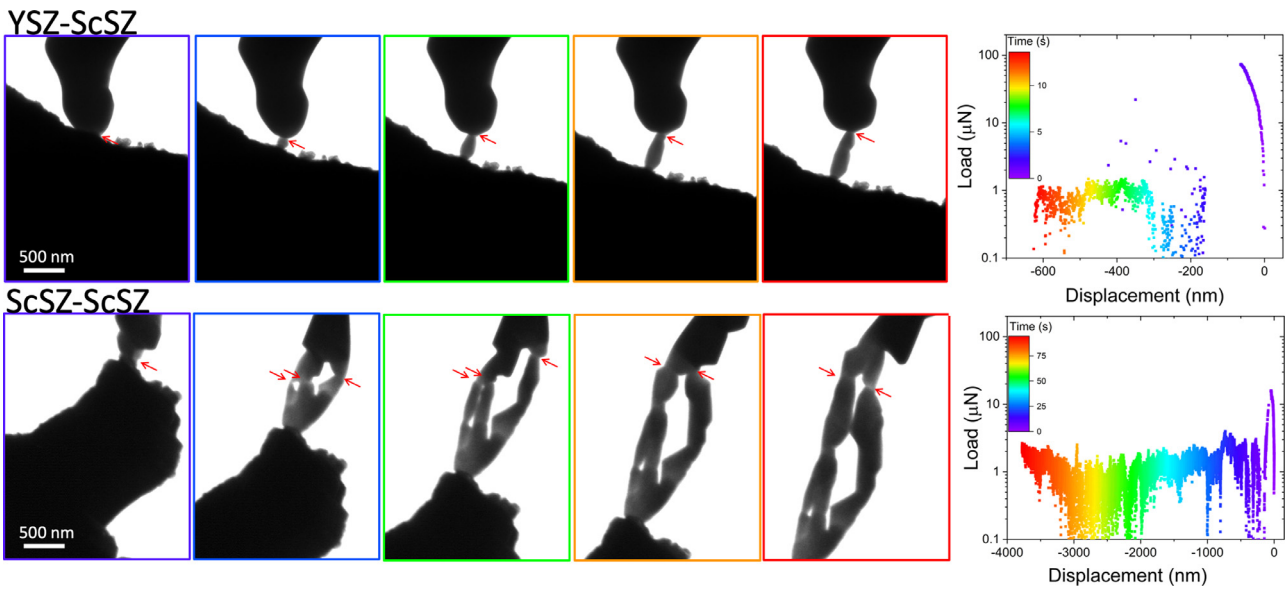

Fig. 1. Example constant displacement rate experiments performed at 40 nm s^{-1} on YSZ-ScSZ and ScSZ-ScSZ at T=1928 °C and T=1975 °C, respectively. The YSZ-ScSZ were performed with a 30s pre-anneal after bicrystal formation that enables the formation of a larger neck and results in an initially higher strength, as seen in the load-displacement curves. The grain boundaries are highlighted by red arrows. Coble creep via diffusion from the surface into the grain boundary results in the formation of the nanowire-like features. Due to the small area of the grain boundary neck, the associated loads are comparable to the accuracy of the measurement ≈1 μN, which has a precision ≈0.2 μN. Note that the color scale represents time and starts at the onset of tensile displacement.

°C, respectively, and under identical constant displacement rates, $\dot{l}$= 40 nm s^{-1}; also see Videos S1 and S2. The former sample was allowed to pre-sinter for > 30 s while the latter was tested immediately after contact. The pre-sintered asperity contact forms a larger neck. Under tensile displacement the load increases rapidly prior to grain boundary fracture. The grain boundary tensile fracture strength, $\sigma_{gb} \approx 0.5 - 1.9$ GPa, is somewhat independent of temperature but sensitive to strain rate when brittle fracture occurs prior to grain boundary yeilding; as discussed in further detail in the companion paper [38]. In a fraction of the YSZ-ScSZ samples tested, a new neck formed after fracture. This occurs due to the small hysteresis in the displacement control after a fracture event that brings the two crystals slightly back into contact. New contacts formed only in ≈ 20% of the YSZ-ScSZ experiments. Upon formation of a new neck, continued displacement resulted in the formation of elongated nanowire-like structures at stresses more than one order of magnitude lower than either the grain boundary fracture stress or the compressive yield strength measured at similar temperatures [43]. For the samples not given any time to pre-sinter, an initial transient in load exists, but the grain boundary typically does not fracture. These samples similarly form one or multiple nanowire-like structures that grow in length during displacement at relatively low stresses; i.e. well below the bulk yield stress or grain boundary fracture stress. The authors are only aware of a single prior report of a similar grain boundary mediated nanowire growth phenomenon. [56] In that work a cluster of nanoparticles formed a nanowire during Joule heating from a probe contact, but it was suggested that the wire grew under compression rather than tension. [56] A similar mechanistic idea, Coble creep referred to as 'pseudo-elasticity', has been invoked to understand the contact induced deformation response of metallic nanoparticles studied both in situ and ex situ. [57,58] In our latter experiments, the nanowire-like structures formed in every experiment performed within a certain range of displacement rates. Multiple nanowires often evolved in parallel when the samples were tested under these conditions, because multiple pre-existing point contacts could all induce nanowire growth. Single nanowires only formed when the samples were pre-sintered, since the initial brittle fracture only produced single point contacts after fracture and only in ≈20% of the experiments. During the formation of the nanowires the grain boundaries may be observed through the presence of surface triple junctions that form measurable dihedral angles and the reduced thickness contrast when the boundary is near an edge on condition. The boundaries are quite dynamic during the process; both migrating along the length of the nanowire and varying in grain boundary plane orientation; e.g. see Video S3. The mechanical tester must return to its initial position at the end of the experiment, which typically destroys the nanowire structure and reconsolidates it into the tip. At the end of each test, sintering and surface diffusion facilitate the formation of a new asperity of the same orientation that can be used in subsequent experiments; smoothing of asperities is discussed below in the context of measuring surface diffusivity. This phenomenon makes this approach very efficient in obtaining large experimental data sets.

Fig. 2a shows images obtained from a series of tensile experiments performed at various temperatures and loading rates, which will subsequently be referred to as "nanowire-growth" experiments. The average neck width at the grain boundary position measured as a function of displacement rate and temperature is shown in Fig. 2b. The parabolic relationship between neck width and displacement rate suggests a diffusion-controlled process; specifically grain boundary diffusion. Neck width is used as the primary measure, because surface energy anisotropy can cause the shape of the nanowire cross-section to evolve over time. The neck width does not necessarily have to be isometric due to anisotropic diffusion in-plane, however the approximate parabolic scaling observed in Fig. 2b measured over multiple experiments at random misorientations suggests that the assumption of an approximately circular neck is reasonable. Coble creep describes the strain rate, $\dot{\varepsilon}$, of a polycrystal during creep;

$$\dot{\varepsilon} = \frac{J\,V_m}{d} \tag{4}$$

where d is the grain size and J is the atomic flux;

$$J = A\frac{\delta}{d^2}\frac{\sigma}{RT}D_{gb} \tag{5}$$

Here, R is the gas constant, T is temperature, σ is the stress, and δ is the grain boundary thickness. The analysis used herein

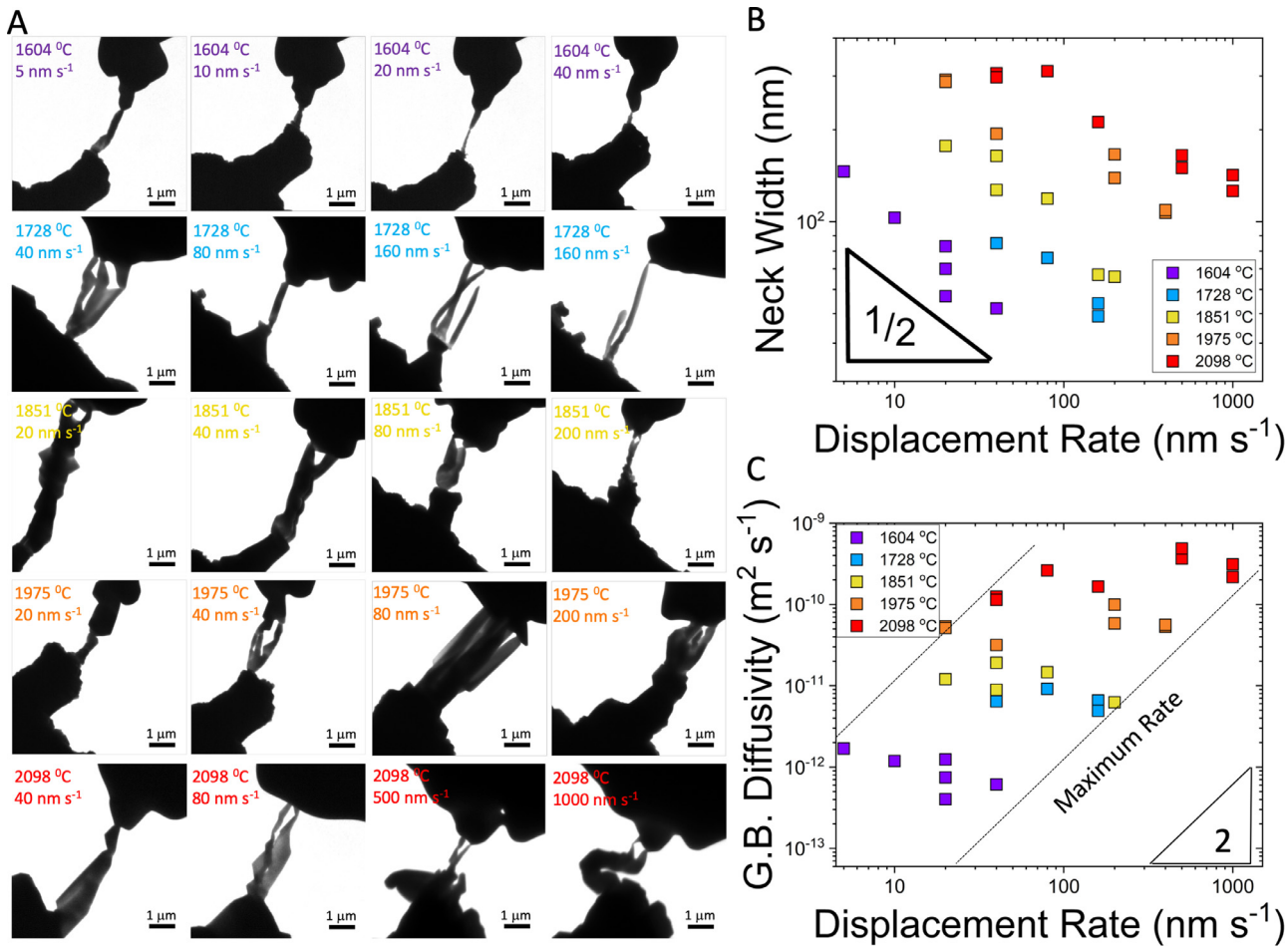

Fig. 2. A) Example images taken from ScSZ-ScSZ experiments performed at different temperatures and displacement rates. The resulting data are used to plot B) the average neck width versus displacement rate and C) the average grain boundary diffusivity versus displacement rate.

considers the time constant, t_c, associated with inserting a single atomic plane into a grain boundary neck with a circular cross section, which is taken to be the displacement rate divided by the Burger's vector. This yields a similar equation for 2-D diffusion in the grain boundary at steady-state;

$$D_{gb} = {}^{x^2 RT}/_{2\pi t_c \sigma V_m} \tag{6}$$

where x is the neck radius. In each experiment, an average value of x is obtained from 5 to 10 measurements made at random times. A combination of surface diffusion and grain boundary sliding could also cause similar nanowire growth. If this process were dominant then the wires should grow at large angles off axis, which is not the case. Furthermore, grain boundary diffusivity was determined independently via separate experiments, as discussed in the companion paper [38], and those results are in good agreement with values calculated from this data. Therefore, diffusion is taken to be the dominant mechanism. The force values measured from creep deformation of the small nanowire-like features formed are small relative to the accuracy of the instrumentation, $\approx 1\ \mu$N. AA A contact force evolves upon initial contact of the indenter to the sample, which makes it difficult to define zero load at the μN level. In order to avoid introducing random errors, the nominal sintering stress, $\sigma_s = {}^{2\gamma}/_{r}$, where r is the radius of the wire, is taken as the stress on the neck but as a tensile stress rather than a compressive stress. In certain samples, the unloading curve is stress-free, in which case the zero load can be well defined at each position of displacement. In these cases, the stress during nanowire formation is a factor of 2 lower than σ_s. Johnson-Kendall-Roberts contact mechanics theory in the reversible elastic regime predicts an adhesion stress of $\sigma_{ad} = {}^{3\gamma}/_{r}$.[59] This value has been obtained for fracture of nanoscale Au grain boundaries at high displacement rates. [60] It is found from constant load experiments, discussed in the companion paper [38], that when the applied stress exceeds the sintering stress by more than a factor of 2 the samples are inherently unstable. Furthermore, the energy dissipated due to surface formation and due to irreversible entropy are experimentally isolated, and it is found that the surface energy term dominates when the stress is less than $\approx 5\sigma_s$, assuming linear extrapolation to this relatively higher stress. Since energy dissipation is primarily through the surface energy term, the error introduced by the assumption that $\sigma = \sigma_s$ will be systematic and should be less than a factor of 2 when in steady-state.

Calculated grain boundary diffusivities for the ScSZ-ScSZ samples presented in Fig. 2c exhibit no appreciable displacement rate dependence. Experiments were performed across a range of displacement rates. At high displacement rates, the nanowires rapidly taper down and pinch off, ceasing to grow rather than reach a steady-state. This imposes an upper bound on the measurement. As shown in Fig. 2c, an approximately parabolic relationship between the maximum displacement rate and the diffusivity exists, which is consistent with diffusion limited kinetics. A minimum displacement rate also bounded the ScSZ-ScSZ nanowire growth experiments. At sufficiently low rates nanosheets formed rather than nanowires. This could be confirmed during unloading, where some sheets would twist and their thickness would be observable. This

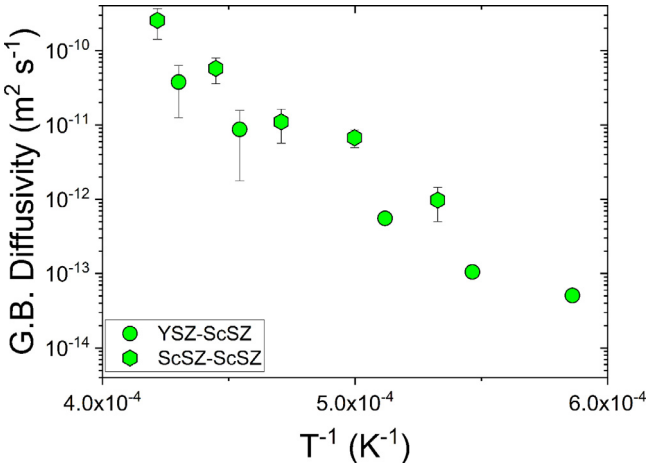

Fig. 3. Arrhenius plot of the grain boundary diffusivity versus temperature for YSZ-ScSZ and ScSZ-ScSZ samples determined from the growth of the nanowire-like features during Coble creep.

nanowire shape anisotropy is clearly visible in Video S3 when the sample loaded at 80 nm s^{-1} is unloaded and the its thickness can be observed as it rotates. The minimum rate was somewhat sensitive to initial contact geometry as confirmed by performing multiple experiments at the same displacement rates. Despite these variations, the relationship between the minimum displacement rate and the diffusivity also appears to follow somewhat parabolic scaling. The breakup of sheets into wires is observed in several experiments and should involve a Rayleigh instability that has some characteristic distance defined by the rate limiting diffusivity. This instability is also a possible source of multiple nanowires observed in the ScSZ-ScSZ experiments; for example see Video S3.

The grain boundary diffusivities from both sample sets are plotted in Fig. 3. The data agree well despite the small differences in chemistry and the measurement of a fixed set of high-angle bicrystals in the YSZ-ScSZ sample versus random grain boundaries in the ScSZ-ScSZ samples. Large grain boundary diffusion anisotropy is commonly observed in tracer diffusivity experiments with somewhat stationary boundaries. [61] In our experiments, the grain boundary plane orientation varies significantly during the experiment. Grain boundary energies vary strongly with grain boundary plane orientation, even for the case of misorientations with a high coincidence of lattice sites. [62,63] Thus, the measurements here represent an average of multiple configurations that likely provides a measurement somewhat representative of general boundaries in the system. The variation in grain boundary plane and the associated variations in instantaneous diffusivity likely account for much of the experimental uncertainty captured by the error bars. Local variations in temperature as a function of time and local geometry, however, could contribute to the experimental uncertainty. Similarly, the assumption of axial geometric symmetry could also contribute to the uncertainty. These latter factors are difficult to assess. The average grain boundary diffusivities for the two sample sets are described by $D_{gb}^{ScSZ-ScSZ} = (0.056 \pm 0.05)\exp(\frac{-380{,}000 \pm 40{,}000}{RT}) m^2\ s^{-1}$ and $D_{gb}^{YSZ-ScSZ} = (0.0039 \pm 0.0014)\exp(\frac{-360{,}000 \pm 32{,}000}{RT}) m^2\ s^{-1}$. The data are Arrhenius between 1433 °C and 2098 °C. The Arrhenius behavior suggests no change in mechanism occurs in this range. Oxygen grain boundary tracer diffusion has mainly been measured at considerably lower temperatures, where it exceeds cation tracer measurements by several orders of magnitude and has an activation energy ≈25-35% of the cation value; see Figure S3. Extrapolating various low temperature anion values to high temperatures suggests that they could intersect measured cation values between T ≈ 1450 °C and T > T^{melt}. The Arrhenius behavior, having an activation energy consistent with cation tracer measurements, suggests that our results should be interpreted as measurements of cation transport. Furthermore, since cation diffusivity for both yttrium and scandium exceeds the rate of self-diffusion, [64] the results are interpreted primarily as zirconium cation diffusion limited. It has been suggested that zirconium cation diffusion in the lattice is mediated by an anion-cation vacancy pair. [65].

4.2. Phase-field simulation results for single grain boundary creep

Fig. 4 shows that the simulated spatial distribution of oxygen vacancies, scandium defects, and hydrostatic stress distribution of ScSZ indenter and ScSZ substrate after 30s of pre-annealing, at 1975°C. The grain boundary core and the surfaces of the two-grain system are both rich in oxygen vacancies (see Fig. 4a) and attract negative scandium defects to the structural core (see Fig. 4b). The positive oxygen vacancies at the interfaces induce both an oxygen and a scandium depletion zone in front of interfaces as a result of the electrostatic attraction of $[Sc'_{Zr}]$ and $[V_O^{\cdot\cdot}]$. In addition, the grain boundary triple junctions are more structurally disordered

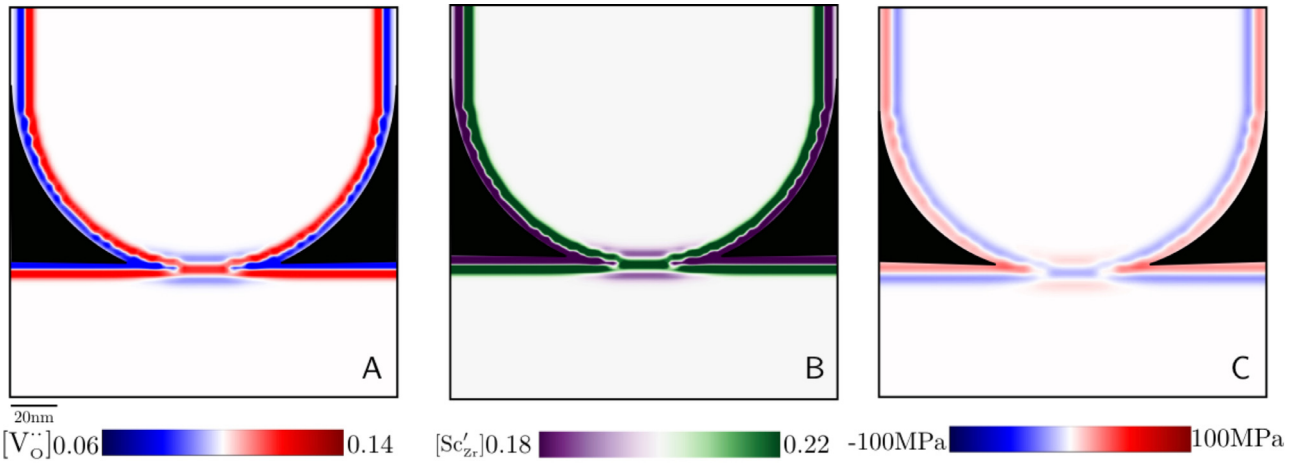

Fig. 4. The microstructure of ScSZ indenter and ScSZ substrate (gray box (II) of Fig. 10) was pre-annealed for 30s at T=1975°C. A shows $[V_O^{\cdot\cdot}]$ distribution, B shows $[Sc'_{Zr}]$ distribution, and C shows hydrostatic stress distribution. The grain boundary and free surfaces accumulate $[V_O^{\cdot\cdot}]$ due to structural and chemical driving forces, which in turn naturally attracts $[Sc'_{Zr}]$ due to its opposite charge polarity. The accumulated $[Sc'_{Zr}]$ defects at the interfaces expand the zirconia lattice and imposes a compressive hydrostatic stress.

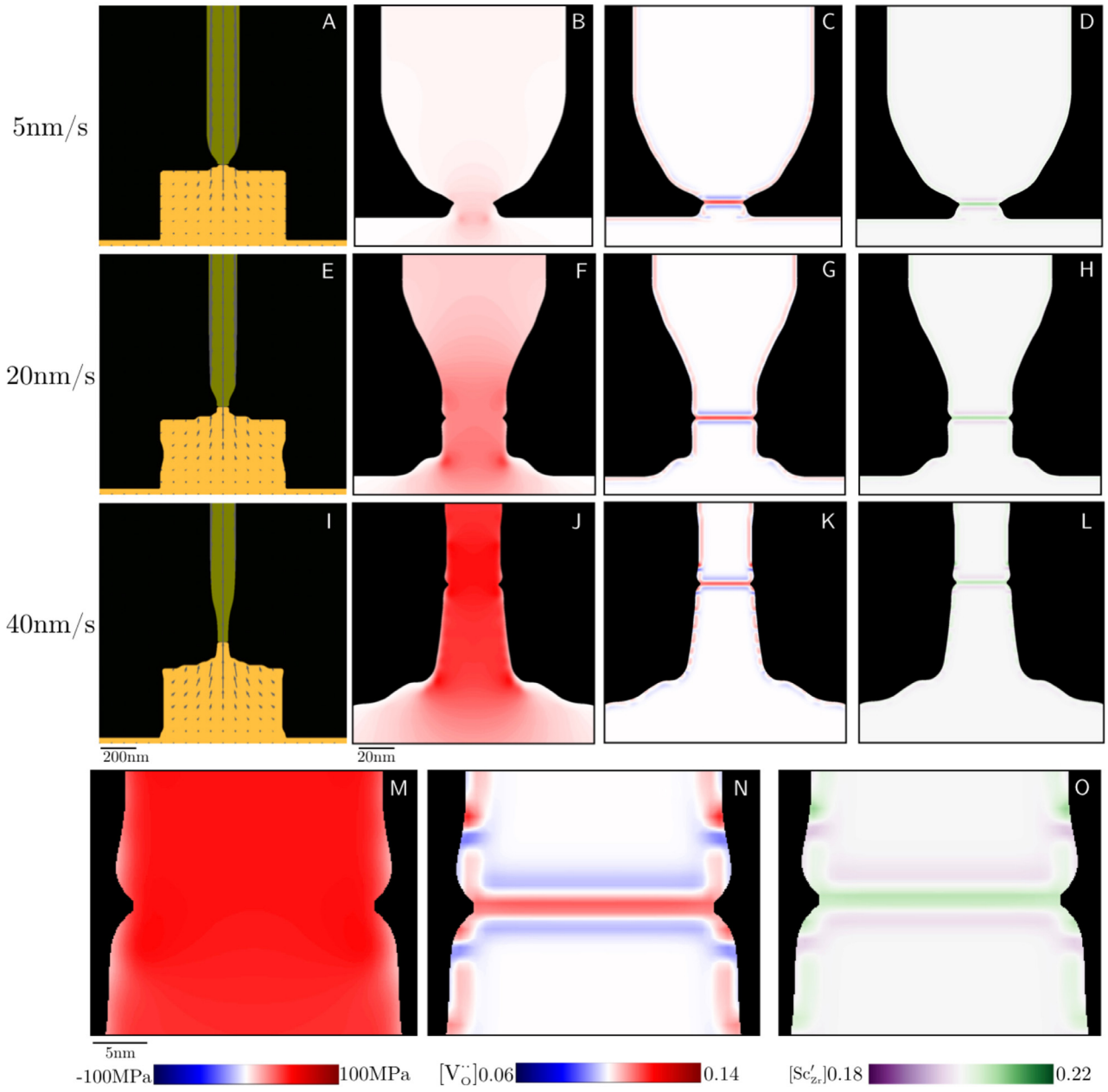

Fig. 5. Defect distribution and hydrostatic stress distribution for a ScSZ indenter-ScSZ substrate system after a 30s pre-annealing step (gray box (II) of Fig. 10), at T=1975°C, now subjected to 5 nm s^{-1}, 20 nm s^{-1} and 40 nm s^{-1} to displacement rates. M, N, and O show a magnified view at triple junctions for hydrostatic stress, oxygen vacancies, and scandium defects distribution for $\bar{v}$=40 nm s^{-1}.

than surfaces and grain boundaries and accumulate larger amounts of $[Sc'_{Zr}]$ and $[V^{\cdot\cdot}_{O}]$. The chemical expansion coefficient of scandium defects induces a compressive stress ~20MPa in the grain boundary core as well as below the surrounding free surfaces (see Fig. 4c). To enforce mechanical equilibrium, a weakly tensile region near the oxygen vacancy depletion region forms. In the present study, two major species are mainly considered; $[V^{\cdot\cdot}_{O}]$ and $[Sc'_{Zr}]$. The concentration of Zr vacancies, $[V'''_{Zr}]$, is anticipated to be 2-3 orders of magnitude smaller than $[V^{\cdot\cdot}_{O}]$ and $[Sc'_{Zr}]$ based on experiments and DFT calculations. [66–68]. Therefore, $[V^{\cdot\cdot}_{O}]$ and $[Sc'_{Zr}]$ defects are anticipated to dominate grain boundary thermodynamics despite the expectation that $[V'''_{Zr}]$ are rate-limiting for grain boundary diffusion kinetics.

The effect of tensile displacement rate is summarized in Fig. 5 for a macroscopic crystallographic misorientation of $\Delta\theta = 22.5^{\circ}$. For 5 nm s^{-1} (see Fig. 5a), the stress gradients (see Fig. 5b) induce the development of a contact neck as a result of mass being pushed from the substrate grain to the indenter through the grain boundary, which results in nanowire growth. The asymmetric stress distribution near the grain boundary induces an asymmetric grain boundary groove and free surfaces dihedral angle, $\Psi = 83.62^{\circ}$, which deviates from the equilibrium dihedral angle, $\Psi_{eq} = 102^{\circ}$, defined in the model. This asymmetry drives grain boundary migration in the direction of the imposed displacement. As compared to a pre-annealed sample not yet loaded in tension, Figs. 5c and 5d demonstrate that the local segregation of oxygen vacancies and scandium defects decreases.

For intermediate tensile displacement rates, e.g., 20 nm s^{-1} (see Fig. 5e), the spatial extent of the hydrostatic stress gradients increases, which in turn drives more mass from the surface to the grain boundary enhancing the elongation of the nanowire near the grain boundary (see Fig. 5f). The neighboring surfaces develop

a concentration of oxygen vacancies that is lower than the grain boundary core (see Fig. 5g); however, corner effects (triple junctions) dominate the segregation of the interface and shift the $[Sc'_{Zr}]$ to a preferential corner (see Fig. 5h). Further, the $[Sc'_{Zr}]$ defects cannot keep up with the moving grain boundary, resulting in a decrease of $[Sc'_{Zr}]$ in the grain boundary core, followed by the appearance of a small depletion zone adjacent to the grain boundary. In addition, the vicinity of contact areas with negative radius of curvature become more defect concentration depleted. Here, as the boundary moves, diffusion is large enough to bring the extent of the depletion zone in front of the grain boundary back to equilibrium, thus enabling a symmetric distribution of defects in the vicinity of the grain boundary as reported in recent work [69,70].

For large tensile displacement rates, e.g., 40 nm s^{-1} (see Fig. 5i), the hydrostatic stress increases in the necking region, which favors larger mass fluxes from the substrate to the indenter and thus the neck becomes thinner (see Fig. 5j), in qualitative agreement with the experimental results, see Fig. 2. The surfaces in the neck portion below the grain boundary develop a smaller amount of oxygen vacancies than the surfaces above the grain boundary (see Fig. 5k and n). This is due to stress-driven mass flux in the necking region. Also, the fast moving (externally stressed) interfaces result in a drastic decrease of scandium defects on the surrounding surfaces because of its low diffusivity (see Fig. 5l). Further, the preferential segregation of scandium defects (see Fig. 5o) at structurally disordered triple junctions relaxes the lattice and thus decreases the tensile stress (see Fig. 5m). The simulations reproduce the general nanowire growth response and morphology resulting from single grain boundary Coble Creep. The goal of these simulations is to primarily demonstrate the phenomenology can be reproduced based on physical parameters reported in the literature, and predict general trends related to local chemistry that are difficult to obtain from the *in situ* experiments. For example, within the range of experimental parameters tested the model predicts rare-earth segregation and the development of a space charge layer occurs in all cases, but with concentrations and distributions sensitive to the local thermo-kinetic interactions. This supports the inherent assumption in the experimental analysis, in both this manuscript and the companion paper, that the dominate diffusion mediating defect is consistent across the range of displacement rates and stresses measured.

4.3. Surface diffusivity from capillary smoothing

Typically, each nanowire-growth experiment ends with a configuration containing high curvature features formed after recompression of the nanowire. Knowledge of the surface diffusivity is practically useful in predicting the stability of nanowires grown. From the rate of capillary smoothing it is possible to calculate the surface diffusivity following the analysis of Nichols and Mullins. [71] They described the evolution of the radius of curvature, r, and the position, z, of conical tips using the following relations;

$$r_t^4 - r_{t,o}^4 = A_\alpha \frac{D_s \gamma_s V_m \nu}{kT}(t - t_o) \tag{7}$$

and

$$z_t^4 - z_{t,o}^4 = B_\alpha \frac{D_s \gamma_s V_m \nu}{kT}(t - t_o) \tag{8}$$

where A_α and B_α are independent geometric factors that both depend on the cone half-angle, ν is the concentration of surface diffusion mediating defects, D_s is the surface diffusivity, t is time, and $\gamma_s = 1.34$J m^{-2} is the surface energy, whose values is determined for ScSZ-ScSZ samples from related experiments discussed in the companion paper. [38] Fig. 6a and Video S4 show an example of an asperity smoothing experiment where both the tip radius of curvature and tip position follow the anticipated quartic time dependence. Using both measures allows for the determination of a consistent set of A_α and B_α constants, which are generally found to be in reasonable agreement with direct measurement of the cone half-angle associated with the protrusions, see Fig. 6b. Fig. 6c plots the surface diffusivities measured as a function of temperature. The measurement is averaged over many surface orientations and thus provides an average value for the system. The experimental uncertainty is anticipated to reflect variations caused by anisotropy, although as noted above the results could be affected by the assumption of axial symmetry and small local variations in temperature. The calculated surface diffusivity is $D_s = (0.10 \pm 0.27)\exp(\frac{-380{,}000 \pm 28{,}000}{RT}) m^2\ s^{-1}$.

Fig. 7 compares the grain boundary and surface diffusivities obtained in this study to prior results of zirconium tracer diffusion, cation tracer diffusion, and interdiffusion in ZrO_2 reported in the literature. [34,72–81] The grain boundary values of cation diffusion measured in our work are intermediate to trends reported in the literature. Significant scatter exists in the literature data, however some of this may be rationalized. For example, several reported values were calculated using lattice diffusion constants obtained from their polycrystalline interdiffusion experiments. [24,31] This type of data fitting can be subject to a variety of errors, and in certain examples the resulting lattice diffusion coefficients exceed single crystal tracer values obtained from samples of similar chemistry by more than 3 orders of magnitude. [64] The primary goal here is not to review all of the literature in detail, but instead is to highlight that our results generally agree with the majority of those data to within about an order of magnitude. The current results, furthermore, do not depend on knowledge of $D_{lattice}$.

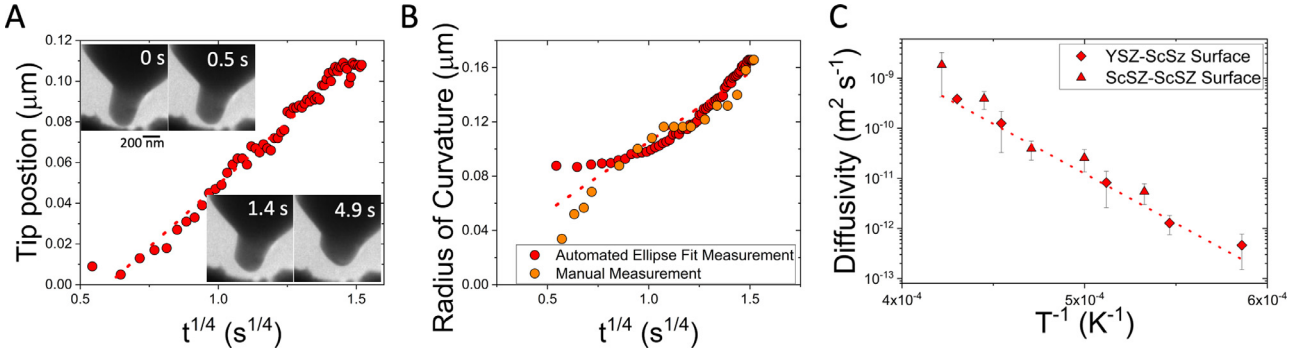

Fig. 6. An example of an asperity smoothing experiment performed on 10ScSZ demonstrating quadric kinetics in both A) the tip position and B) the radius of curvature used to calculate surface diffusivity. C) Arrhenius plot of the surface diffusivity versus temperature for YSZ-ScSZ and ScSZ-ScSZ experiments. Note that for B) the elliptical fitting routine used to measure the data slightly overestimates the radius of curvature at the initial times, which is confirmed through manual measurements that are also plotted in B).

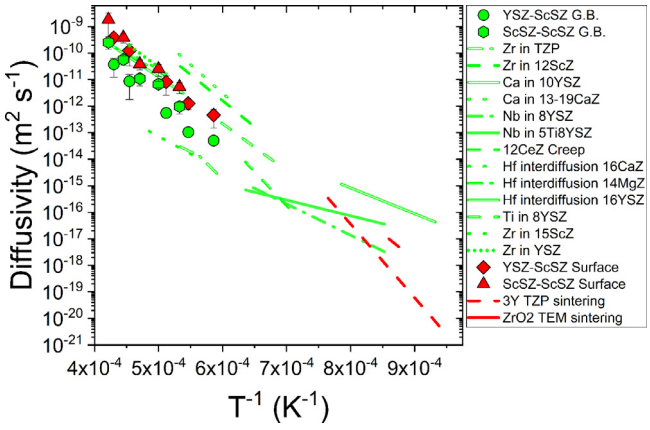

Fig. 7. Comparison of grain boundary and surface diffusivities measured in this study (red) with literature values (green), where tracer diffusion experiments are assumed to have a grain boundary width of 1 nm. Reference data from [34,72–81]

Few reports of cation surface diffusivity in ZrO_2 exist and measurements have primarily been obtained at lower temperatures. The two relevant data in Fig. 7 were measured from TZP and a mixture of tetragonal and monoclinic ZrO_2. [79,80] Those studies measure dramatically different activation energies, but comparable magnitudes of diffusion at comparable temperatures. Although the existing surface diffusion data do not provide an excellent basis for comparison, overall our data extrapolates well towards those values obtained from ZrO_2 samples of different chemistry and phase. Our measurements of interfacial diffusivity are comparable, where $D_s \approx 2\text{-}3D_{gb}$ for the ScSZ-ScSZ and YSZ-ScSZ experiments. Surprisingly few investigations have attempted to measure surface and grain boundary diffusivity within a single study. Johnson et al. compared surface and grain boundary diffusivities, and determined that the magnitudes were comparable. [82] Recent molecular dynamics simulations performed using a Ni potential reported $D_s \approx \frac{1}{2}D_{gb}$. [83] For reference, Figure S4 compares grain boundary and surface measurements reported for Ni and Cu in a series of separate experiments, which produce values of $D_s \approx 2\text{-}3D_{gb}$. [84–87] Surface diffusivity is highly sensitive to environment and adsorption; thus it is more ideal to compare under similar experimental conditions. Our results regarding the relative rates of surface and grain boundary diffusion, nevertheless, appear to agree with broader trends reported in the literature. As discussed above the neck width scales parabolically with displacement suggesting grain boundary diffusion is the rate limiting mechanism. However, the magnitude of the diffusivities is comparable. One explanation for grain boundary diffusion being rate limiting, is the fact that the grain boundary tends to remain near the asperity tip being displaced such that the diffusion distance between the source material and grain boundary remains relatively short. In fact, in several cases where the grain boundary remains at the middle of the nanowire, the neck width tends to reduce and pinch-off. At these temperatures the grain boundaries can be highly mobile, and it is noted that similar grain boundary motion is observed in phase-field simulations.

5. Conclusion

Through a combination of high temperature in situ nanomechanical testing experiments and phase field simulations it is demonstrated that tensile Coble creep results in solid-state nanowire growth. The experiments also produce a robust set of measurements of interface diffusivity; grain boundary diffusion during the experiments and surface diffusion measured from subsequent capillary relaxations. Surface diffusivity was found to exceed grain boundary diffusivity by a comparable amount as has been reported for other crystalline systems, although it is noted that few examples exist where both values were measured experimentally in a single study.

Contributions

R.L. Grosso prepared the 10ScSZ samples for testing in collaboration with E.N.S. Muccillo, D.N.F. Muche, and R.H.R. Castro, and assisted with experimental data analysis. L. Feng and G.S. Jawaharram also helped complete the experimental data analysis. C.M. Barr and A.M. Monterrosa helped perform high temperature experiments. K. Hattar and S.J. Dillon oversaw the experimental aspects of this work. K.S.N. Vikrant perfomed the reported phase-field work and associated analysis under the supervision of R.E. García.

Declaration of Competing Interest

The authors declare that they have no known competing financial interests or personal relationships that could have appeared to influence the work reported in this paper.

Acknowledgements

Support from National Science Foundation under Grant No. DMR 1922867 is acknowledged by SJD. RG and EM gratefully acknowledge FAPESP (2016/06205-1 and 2017/25501-3), CAPES (Finance code 001), and CNPq (305889/2018-4) for the financial support. DM acknowledges CNPq (236631/2012-8). Support from the Army Research Office Grants W911NF1810361 and W911NF1710026 are acknowledged by RC. K.S.N. Vikrant and R.E. García thank the support provided by US ONR N00014- 17-1-2087. This work was carried out in part in the Frederick Seitz Materials Research Laboratory Central Research Facilities, University of Illinois at Urbana-Champaign. CMB and KH were supported by the DOE-BES Materials Science and Engineering Division under FWP 15013170. This work was performed, in part, at the Center for Integrated Nanotechnologies, an Office of Science User Facility operated for the U.S. Department of Energy (DOE) Office of Science. Sandia National Laboratories is a multi-mission laboratory managed and operated by National Technology & Engineering Solutions of Sandia, LLC, a wholly owned subsidiary of Honeywell International, Inc., for the U.S. DOE's National Nuclear Security Administration under contract DE-NA-0003525. The views expressed in the article do not necessarily represent the views of the U.S. DOE or the United States Government.

Supplementary materials

Supplementary material associated with this article can be found, in the online version, at doi:10.1016/j.actamat.2020.08.069.

References

[1] R.L. Coble, A Model for Boundary Diffusion Controlled Creep in Polycrystalline Materials, J. Appl. Phys. 34 (6) (1963) 1679–1682.
[2] M.F. Ashby, R.A. Verrall, Diffusion-accommodated flow and superplasticity, Acta Met. 21 (2) (1973) 149–163.
[3] B. Mandl, et al., Growth Mechanism of Self-Catalyzed Group III-V Nanowires, Nano Lett 10 (11) (2010) 4443–4449.
[4] O. Moutanabbir, et al., Colossal injection of catalyst atoms into silicon nanowires, Nature (London, U. K.) 496 (7443) (2013) 78–82.
[5] C.W. Hewson, W.D. Kingery, Effect of magnesium oxide and magnesium titanate doping on diffusion-controlled creep of polycrystalline aluminum oxide, J. Am. Ceram. Soc. 50 (4) (1967) 218–219.
[6] R.L. Coble, Y.H. Guerard, Creep of polycrystalline aluminum oxide, J. Am. Ceram. Soc. 46 (1963) 353–354.

[7] O.A. Ruano, J. Wadsworth, O.D. Sherby, Deformation of fine-grained alumina by grain boundary sliding accommodated by slip, Acta Mater 51 (12) (2003) 3617–3634.
[8] C. Herring, Effect of change of scale on sintering phenomena, J. Appl. Phys. 21 (1950) 301–303.
[9] Y. Arachi, et al., Electrical conductivity of the ZrO2-Ln2O3 (Ln = lanthanides) system, Solid State Ion. 121 (1-4) (1999) 133–139.
[10] H.H. Moebius, Oxygen-ion-conducting solid electrolytes and their ap- plications. Oxygen-ion conductance of solids and the unipolar ionic conductance in the fluorite structures, Z. Chem. 2 (4) (1962) 100–106.
[11] E.C. Subbarao, H.S. Maiti, Solid electrolytes with oxygen ion conduction, Solid State Ion. 11 (4) (1984) 317–338.
[12] D.R. Clarke, Materials selection guidelines for low thermal conductivity thermal barrier coatings, Surf. Coat. Technol. 163-164 (2003) 67–74.
[13] P.F. Manicone, P. Rossi Iommetti, L. Raffaelli, An overview of zirconia ceramics: Basic properties and clinical applications, J. Dent. 35 (11) (2007) 819–826.
[14] M. Ahrens, et al., Sintering and creep processes in plasma-sprayed thermal barrier coatings, J. Therm. Spray Technol. 13 (3) (2004) 432–442.
[15] D. Dimos, D.L. Kohlstedt, Diffusional creep and kinetic demixing in yttria-stabilized zirconia, J. Am. Ceram. Soc. 70 (8) (1987) 531–536.
[16] D. Gomez-Garcia, et al., Mechanisms of high-temperature creep of fully stabilized zirconia single crystals as a function of the yttria content, J. Am. Ceram. Soc. 80 (7) (1997) 1668–1672.
[17] A. Lakki, et al., Mechanical loss, creep, diffusion and ionic conductivity of ZrO2-8 mol%Y2O3 polycrystals, J. Eur. Ceram. Soc. 20 (3) (2000) 285–296.
[18] D. Zhu, R.A. Miller, Sintering and creep behavior of plasma-sprayed zirconia- and hafnia-based thermal barrier coatings, Surf. Coat. Technol. 108-109 (1-3) (1998) 114–120.
[19] M. Friis, C. Persson, J. Wigren, Influence of particle in-flight characteristics on the microstructure of atmospheric plasma sprayed yttria stabilized ZrO2, Surf. Coat. Technol. 141 (2-3) (2001) 115–127.
[20] S.Y. Park, et al., Microscopic observation of degradation behavior in yttria and ceria stabilized zirconia thermal barrier coatings under hot corrosion, Surf. Coat. Technol. 190 (2-3) (2004) 357–365.
[21] Y. Dong, Inversion of oxygen potential transitions at grain boundaries of SOFC/SOEC electrolytes, arXiv.org, e-Print Arch., Condens. Matter (2018) 1–20.
[22] M. Cologna, B. Rashkova, R. Raj, Flash sintering of nanograin zirconia in <5 s at 850°C, J. Am. Ceram. Soc. 93 (11) (2010) 3556–3559.
[23] M.J. Verkerk, A.J.A. Winnubst, A.J. Burggraaf, Effect of impurities on sintering and conductivity of yttria-stabilized zirconia, J. Mater. Sci. 17 (11) (1982) 3113–3122.
[24] Y. Oishi, H. Ichimura, Grain boundary-enhanced interdiffusion in polycrystalline calcium oxide-stabilized zirconia system, J. Chem. Phys. 71 (12) (1979) 5134–5139.
[25] M.A. Taylor, et al., 96Zr diffusion in polycrystalline scandia stabilized zirconia, J. Eur. Ceram. Soc. 25 (9) (2005) 1591–1595.
[26] T. Bak, et al., Grain boundary diffusion of magnesium in zirconia, J. Am. Ceram. Soc. 85 (9) (2002) 2244–2250.
[27] V.M. Bekale, et al., Impurity diffusion of cerium and gadolinium in single- and polycrystalline yttria-stabilized zirconia, Philos. Mag. 88 (1) (2008) 1–19.
[28] K. Kowalski, A. Bernasik, A. Sadowski, Diffusion of calcium in yttria stabilized zirconia ceramics, J. Eur. Ceram. Soc. 20 (12) (2000) 2095–2100.
[29] K. Kowalski, A. Bernasik, A. Sadowski, Bulk and grain boundary diffusion of titanium in yttria-stabilized zirconia, J. Eur. Ceram. Soc. 20 (7) (2000) 951–958.
[30] M. Matsuda, et al., Lattice and grain boundary diffusion of Ca in polycrystalline yttria-stabilized ZrO2 determined by employing SIMS technique, Solid State Ion. 111 (3,4) (1998) 301–306.
[31] Y. Sakka, et al., Cation interdiffusion and phase stability in polycrystalline tetragonal ceria-zirconia-hafnia solid solution, J. Am. Ceram. Soc. 74 (10) (1991) 2610–2614.
[32] W.H. Rhodes, R.E. Carter, Cationic self-diffusion in calcia-stabilized zirconia, J. Am. Ceram. Soc. 49 (5) (1966) 244–249.
[33] H. Drings, et al., Enhanced 95Zr diffusion in grain boundaries of nano-crystalline ZrO2•9.5 mol% Y2O3, Physica status solidi (a) 206 (1) (2009) 54–58.
[34] M. Matsuda, et al., Lattice and grain boundary diffusion of Ca in polycrystalline yttria-stabilized ZrO2 determined by employing SIMS technique1This work was done while the author was visiting ANSTO.1, Solid State Ion. 111 (3) (1998) 301–306.
[35] L.G. Harrison, Influence of dislocations on diffusion kinetics in solids with particular reference to the alkali halides, Trans. Faraday Soc. 57 (0) (1961) 1191–1199.
[36] A.H. Heuer, Oxygen and aluminum diffusion in α-Al2O3: How much do we really understand? J. Eur. Ceramic Soc., 28 (7) (2008) 1495–1507.
[37] Grosso, R.L., et al., In situ transmission electron microscopy for ultrahigh temperature mechanical testing of ZrO2. Submitted.
[38] Grosso, R.L., et al., Ultrahigh temperature in situ transmission electron microscopy based bicrystal coble creep zirconia ii: interfacial thermodynamics and transport mechanisms. submitted.
[39] R.L. Grosso, E.N.S. Muccillo, R.H.R. Castro, Phase stability in scandia-zirconia nanocrystals, J. Am. Ceram. Soc. 100 (5) (2017) 2199–2208.
[40] R.L. Grosso, et al., Sintering of translucent and single-phase nanostructured scandia-stabilized zirconia, Mater. Lett. 253 (2019) 246–249.
[41] R. Singh, S.B. Chavan, Processing and properties of scandia-doped zirconia electrolyte for intermediate temperature SOFC, ECS Trans. 7 (1) (2007) 2207–2212.
[42] G.S. Jawaharram, et al., Irradiation induced creep in nanocrystalline high entropy alloys, Acta Mater. 182 (2020) 68–76.
[43] Grosso, R.L., et al., In situ transmission electron microscopy for ultrahigh temperature mechanical testing of ZrO2. Nano Lett. 20: p. 1041-1046.
[44] J.-M. Costantini, F. Beuneu, Threshold displacement energy in yttria-stabilized zirconia, Physica status solidi c 4 (3) (2007) 1258–1263.
[45] J. Schindelin, et al., Fiji: an open-source platform for biological-image analysis, Nat. Methods 9 (2012) 676.
[46] A. Fitzgibbon, M. Pilu, R.B. Fisher, Direct least square fitting of ellipses, IEEE Trans. Pattern Anal. Mach. Intell. 21 (5) (1999) 476–480.
[47] K.S.N. Vikrant, W.C. Chueh, R.E. Garcia, Charged interfaces: electrochemical and mechanical effects, Energy Environ. Sci. 11 (8) (2018) 1993–2000.
[48] K.S.N. Vikrant, R.E. García, Charged grain boundary transitions in ionic ceramics for energy applications, npj Comput. Mater. 5 (1) (2019) 24.
[49] Vikrant, K.S.N., et al., Flash sintering incubation kinetics. Submitted, (1): p. 24.
[50] R.E. Garcıá, C.M. Bishop, W.C. Carter, Thermodynamically consistent variational principles with applications to electrically and magnetically active systems, Acta Mater. 52 (1) (2004) 11–21.
[51] F. Larche, J.W. Cahn, Linear theory of thermochemical equilibrium of solids under stress, Acta Met. 21 (8) (1973) 1051–1063.
[52] R. Kobayashi, J.A. Warren, W. Craig Carter, A continuum model of grain boundaries, Physica D 140 (1) (2000) 141–150.
[53] A. Jana, et al., Electrochemomechanics of lithium dendrite growth, Energy Environ. Sci. 12 (12) (2019) 3595–3607.
[54] J.E. Guyer, D. Wheeler, J.A. Warren, FiPy: partial differential equations with python, Comput. Sci. Eng. 11 (3) (2009) 6–15.
[55] A.C.E. Reid, et al., Modelling microstructures with OOF2, Int. J. Mater. Prod. Technol. 35 (3/4) (2009) 361–373.
[56] J.F. Rufner, et al., Local current-activated growth of individual nanostructures with high aspect ratios, Mater. Res. Lett. 2 (1) (2014) 10–15.
[57] A. Sharma, et al., Pseudoelasticity of metal nanoparticles is caused by their ultrahigh strength, Adv. Funct. Mater. 30 (18) (2020) 1807554.
[58] J. Sun, et al., Liquid-like pseudoelasticity of sub-10-nm crystalline silver particles, Nat. Mater. 13 (11) (2014) 1007–1012.
[59] K.L. Johnson, Contact Mechanics, Cambridge University Press, Cambridge, 1985.
[60] N.A. Alcantar, et al., Adhesion and coalescence of ductile metal surfaces and nanoparticles, Acta Mater. 51 (1) (2003) 31–47.
[61] Y. Mishin, C. Herzig, Grain boundary diffusion: recent progress and future research, Mater. Sci. Eng.: A 260 (1) (1999) 55–71.
[62] D.M. Saylor, A. Morawiec, G.S. Rohrer, The relative free energies of grain boundaries in magnesia as a function of five macroscopic parameters, Acta Mater. 51 (13) (2003) 3675–3686.
[63] L. Helmick, et al., Crystallographic Characteristics of Grain Boundaries in Dense Yttria-Stabilized Zirconia, Int. J. Appl. Ceram. Technol. 8 (5) (2011) 1218–1228.
[64] M. Kilo, et al., Cation self-diffusion of 44Ca, 88Y, and 96Zr in single-crystalline calcia- and yttria-doped zirconia, J. Appl. Phys. 94 (12) (2003) 7547–7552.
[65] F.R. Chien, A.H. Heuer, Lattice diffusion kinetics in Y2O3-stabilized cubic ZrO2 single crystals: a dislocation loop annealing study, Philos. Mag. A 73 (3) (1996) 681–697.
[66] Y. Dong, et al., A computational study of yttria-stabilized zirconia: II. Cation diffusion, Acta Mater. 126 (2017) 438–450.
[67] M. Kilo, R.A. Jackson, G. Borchardt, Computer modelling of ion migration in zirconia, Philos. Mag. 83 (29) (2003) 3309–3325.
[68] M. Kilo, et al., Modeling of cation diffusion in oxygen ion conductors using molecular dynamics, Solid State Ion. 175 (1) (2004) 823–827.
[69] Vikrant, K.S.N., W. Rheinheimer, and R.E. García, Electrochemical drag effect on grain boundary motion in ionic ceramics. Submitted.
[70] Vikrant, K.S.N., et al., Electrochemically-Driven abnormal grain growth in ionic ceramics. Submitted.
[71] F.A. Nichols, W.W. Mullins, Morphological Changes of a Surface of Revolution due to Capillarity-Induced Surface Diffusion, J. Appl. Phys. 36 (6) (1965) 1826–1835.
[72] Y. Oishi, Y. Sakka, K. Ando, Cation interdiffusion in polycrystalline fluorite-cubic solid solutions, J. Nucl. Mater. 96 (1) (1981) 23–28.
[73] M.A. Taylor, et al., 96Zr diffusion in polycrystalline scandia stabilized zirconia, J. Eur. Ceram. Soc. 25 (9) (2005) 1591–1595.
[74] K. Kowalski, et al., Diffusion of niobium in yttria-stabilized zirconia and in titania-doped yttria-stabilized zirconia polycrystalline materials, J. Eur. Ceram. Soc. 26 (15) (2006) 3139–3143.
[75] K. Kowalski, A. Bernasik, A. Sadowski, Bulk and grain boundary diffusion of titanium in yttria-stabilized zirconia, J. Eur. Ceram. Soc. 20 (7) (2000) 951–958.
[76] Y. Oishi, H. Ichimura, Grain-boundary enhanced interdiffusion in polycrystalline CaO-stabilized zirconia system, J. Chem. Phys. 71 (12) (1979) 5134–5139.
[77] M. Kilo, et al., Zr and Stabilizer Tracer Diffusion in Calcia- and Yttria-Stabilized Zirconia, ECS Proceedings Volumes 2001-16 (2001) 275–283.
[78] Y. Sakka, Y. Oishi, K. Ando, Zr-Hf interdiffusion in polycrystalline Y2O3-(Zr+Hf)O2, J. Mater. Sci. 17 (11) (1982) 3101–3105.
[79] Akash, M.J. Mayo, Zr surface diffusion in tetragonal yttria stabilized zirconia, J. Mater. Sci. 35 (2) (2000) 437–442.
[80] J. Rankin, B.W. Sheldon, In situ TEM sintering of nano-sized ZrO2 particles, Mater. Sci. Eng. A 204 (1) (1995) 48–53.
[81] H.H. Möbius, H. Witzmann, D. Gerlach, Sauerstoffionenleitende Festelektrolyte und ihre Anwendungsmöglichkeiten; Untersuchungen zur Kationendiffusion im System, Zeitschrift für Chemie 4 (4) (1964) 154–155.
[82] D.L. Johnson, New method of obtaining volume, grain-boundary, and surface diffusion coefficients from sintering data, J. Appl. Phys. 40 (1) (1969) 192–200.
[83] J.M. Sestito, et al., An atomistic simulation study of nanoscale sintering: The role of grain boundary misorientation, Comput. Mater. Sci. 165 (2019) 180–189.

[84] P.S. Maiya, J.M. Blakely, Surface self-diffusion and surface energy of Nickel, J. Appl. Phys. 38 (2) (1967) 698–704.
[85] S.V. Divinski, G. Reglitz, G. Wilde, Grain boundary self-diffusion in polycrystalline nickel of different purity levels, Acta Mater. 58 (2) (2010) 386–395.
[86] F.J. Bradshaw, R.H. Brandon, C. Wheeler, The surface self-diffusion of copper as affected by environment, Acta Metall. 12 (9) (1964) 1057–1063.
[87] T. Surholt, C. Herzig, Grain boundary self-diffusion in Cu polycrystals of different purity, Acta Mater. 45 (9) (1997) 3817–3823.
[88] X. Xia, R. Oldman, R. Catlow, Computational modeling study of bulk and surface of yttria-stabilized cubic zirconia, Chem. Mater. 21 (15) (2009) 3576–3585.
[89] R. Pornprasertsuk, et al., Predicting ionic conductivity of solid oxide fuel cell electrolyte from first principles, J. Appl. Phys. 98 (10) (2005) 103513.
[90] H.A. Abbas, et al., Electrical and dielectric properties of scandia and ceria stabilized zirconia, Can. J. Pure Appl. Sci. 6 (3) (2012) 2161–2167.
[91] P. Gao, et al., Thermal expansion and elastic moduli of electrolyte materials for high and intermediate temperature solid oxide fuel cell, Solid State Ion. 300 (2017) 1–9.